

See discussions, stats, and author profiles for this publication at: <https://www.researchgate.net/publication/226644560>

Spin-vortices and Spin-vortex-induced Loop Currents in the Pseudogap Phase of Cuprates

ARTICLE *in* JOURNAL OF SUPERCONDUCTIVITY AND NOVEL MAGNETISM · NOVEMBER 2011

Impact Factor: 0.91 · DOI: 10.1007/s10948-011-1194-5

CITATIONS

13

READS

21

2 AUTHORS, INCLUDING:



Hiroyasu Koizumi

University of Tsukuba

73 PUBLICATIONS 787 CITATIONS

SEE PROFILE

Spin-vortices and Spin-vortex-induced Loop Currents in the Pseudogap Phase of Cuprates

Ryo Hidekata · Hiroyasu Koizumi

Received: 18 May 2011 / Accepted: 24 May 2011 / Published online: 24 June 2011
© The Author(s) 2011. This article is published with open access at Springerlink.com

Abstract We explain several anomalous phenomena observed in the pseudogap phase of hole-doped cuprates based on the recently proposed spin-vortex superconductivity theory. In this theory, doped-holes become almost immobile small polarons, and spin-vortices are formed with those small polarons as their centers. A Hartree–Fock field for conduction electrons that is optimized for the interaction energy of local moments is derived; it contains a fictitious magnetic field arising from spin-vortices, and yields current carrying states. The obtained currents are loop currents around spin-vortices, i.e., the *spin-vortex-induced loop currents* (SVILCs), and a collection of them produces a macroscopic current. The SVILC explains (1) nonzero Kerr rotation in zero-magnetic field after exposed in a strong magnetic field; (2) the change of the sign of the Hall coefficient with temperature change; (3) the suppression of superconductivity in the $x = 1/8$ static-stripe ordered sample; and (4) a large anomalous Nernst signal, including its sign-change with temperature change. We show that the hourglass-shaped magnetic excitation spectrum is the evidence for the existence of spin-vortices. We further argue that the “Fermi-arc” in the ARPES is a support for the presence of localized moments in the bulk; a disconnected arc-shaped Fermi surface is obtained by assuming an antiferromagnetic interaction between the localized moments in the bulk and itinerant electrons in the surface region.

Keywords Cuprate superconductor · Pseudogap · Spin-vortex · Loop current · Magnetic excitation · Nernst effect · ARPES

1 Introduction

Understanding of the pseudogap phase is believed to be the key to the elucidation of the mechanism of cuprate superconductivity. The polar Kerr-effect measurement has yielded results that strongly suggest the existence of stable loop currents in the pseudogap phase [1, 2]. The recent neutron scattering experiments have reinforced this view by observing magnetic excitations peaked at the two-dimensional momentum $\mathbf{q} = 0$, where the two-dimensionality of the momentum arises from the two-dimensionality of the CuO_2 conduction plane in the cuprate [3].

Currently, there are two types of loop currents that are predicted to exist in the pseudogap phase; one is a circular current within the CuO_4 complex proposed by C. Varma [4], and the other is the *spin-vortex-induced loop current* (SVILC) proposed by one of the present authors [5–8]. The former does not generate a macroscopic current, but the latter does. The scenario for superconductivity using SVILCs explains other phenomena in the pseudogap phase, thus is possible to provide a unified understanding of a variety of cuprate-superconductivity related phenomena.

The appearance of SVILCs requires local moments. Neutron scattering experiments provide evidence for the existence of local moments, where magnetic excitation spectra that indicate the presence of a short-range antiferromagnetic order are obtained; the presence of spin-configurations that cause splitting of the antiferromagnetic peak at low excitation energies are also suggested. The obtained spectrum is called the “hourglass-shaped magnetic excitation spectrum” after its dispersion shape, and the origin of it has been an important issue for the elucidation of the cuprate superconductivity [9–11].

There are two models that explain the hourglass-shaped spectrum. One of them is the *spin-vortex model*; it assumes

R. Hidekata · H. Koizumi (✉)
Institute of Materials Science, University of Tsukuba, Tsukuba,
Ibaraki 305-8573, Japan
e-mail: koizumi@ims.tsukuba.ac.jp

spin configurations with spin-vortices in the antiferromagnetic background in the CuO₂ plane [6, 8, 12]. The other is the stripe model [13]; it assumes the existence of charged-strips and intervening antiferromagnetic-insulator regions in the CuO₂ plane. The spin-vortex model with randomly distributed spin-vortices yields a circular peak that resembles experimental results in a constant energy slice distribution, while the stripe model with static charged-strips yields a rectangular peak [9, 10]. Thus, the spin-vortex model is more satisfactory in this respect. Actually, spin configurations of the spin-vortex model contains those of the strip model as collinear arrangements of spin-vortices, thus as far as the spin configuration is concerned the two models are not so different.

A significant difference between the two is in the way electric current is generated. In the stripe model, charged-stripe regions become rivers of electric current. On the other hand, electric current is generated as SVILCs in the spin-vortex model; thus, it automatically contains the loop-currents that explain the Kerr-effect measurement results.

For the generation of spin-vortices, both strong correlation among electrons and the strong hole-lattice interaction are necessary; due to the latter, doped-holes become almost immobile small polarons at low temperatures, thus the system is in an effectively-half-filled situation (EHFS); then the strong correlation in this effectively-half-filled situation gives rise to local moments. Experiments clearly indicate that the hole-doped cuprate is a system with both strong correlation and strong hole-lattice interaction; the existence of the former is manifested by the fact that the parent compound is a half-filled antiferromagnetic insulator, and the existence of the latter is evidenced in the EXAFS experiments, where Cu-O bonds fluctuations that indicate the small polaron formation are observed below the pseudogap temperature T^* [14].

Since the ground state of a half-filled system with strong correlation is a Mott insulator, one might think that current flow is impossible in the strongly correlated system in the EHFS. However, it has been shown that it is actually possible with the formation of spin-vortices [5–8] by employing the Slater's view that regards the antiferromagnetic insulating state as a band insulator instead of the Mott insulator. Adopting this alternative view is crucial; it means that we do not use the approximation that is used in the derivation of the antiferromagnetic Heisenberg–Hamiltonian from the Hubbard one in the half-filled situation given by

$$c_{j\uparrow}^\dagger c_{j\uparrow}^\dagger + c_{j\downarrow}^\dagger c_{j\downarrow}^\dagger = 1, \quad (1)$$

where $c_{j\sigma}^\dagger$ and $c_{j\sigma}$ are the creation and annihilation operators for electron at the i th site with spin σ , as a substitute for the actual condition

$$\langle c_{j\uparrow}^\dagger c_{j\uparrow}^\dagger + c_{j\downarrow}^\dagger c_{j\downarrow}^\dagger \rangle = 1, \quad (2)$$

where $\langle \hat{O} \rangle$ denotes the expectation value of an operator \hat{O} . The former condition excludes current flow from the beginning, thus may lead to an erroneous conclusion.

If we stick to the condition in (2) and construct the zeroth ground state as a Slater determinant of an extended basis [15], the effectively-half-filled state with current carrying states are obtained. We will call the state constructed by this way the “effectively half-filled Slater state (EHFSS)” [5–8]. If we need more accurate states, they are obtained from the configuration-interaction calculations by treating the EHFSS as the Hartree–Fock solution. The current in the EHFSS is a collection of loop-currents; each of them flows around a spin-vortex with its center at a hole-occupied site. For such currents to generate a macroscopic one, the number density of the spin-vortices has to be sufficiently large.

It has been argued that SVILCs are germs of supercurrent that start to appear in the pseudogap phase [8]. The temperature dependence of the mean-square displacement obtained from EXAFS measurements indicates that small polarons start to appear at T^* , and the number density of them increases with decrease of the temperature [14]. This fact coincides with the STM finding that nanosized local-density-of-state-reduced patches appear below T^* [16], and the region covered by them increases with decrease of the temperature. Further, it is observed that when the whole sample is covered by them, superconductivity occurs [17]. Since the number density of SVILCs is expected to be roughly proportional to the number density of small polarons, the above fact is interpreted that superconductivity occurs when the number density of SVILCs becomes large enough to cover the whole sample.

In contrast to the EXAFS and neutron scattering experiments, the small polaron effect is not apparent in the ARPES results [18]. This fact is explained if small polarons are not formed in the surface region where a large portion of photoelectrons come from. We will show that by adopting the above assumption, the Fermi-arc [19] seen in the ARPES is obtained as a consequence of an antiferromagnetic interaction between itinerant electrons in the surface region and localized moments in the bulk.

This paper is organized as follows. In Sect. 2, we review the mechanism in which the SVILCs appear, succinctly; we will provide a Hartree–Fock field that contains a fictitious magnetic field. The Hartree–Fock field contains $U(2) = U(1) \otimes SU(2)$ parameters, where the $SU(2)$ part is optimized by minimizing the interaction energy between the local moments with prescribed conditions for spin-vortices; and the $U(1)$ part gives rise to the fictitious magnetic field. The compelling evidence for the existence of spin-vortices in the cuprate is the hourglass-shaped magnetic excitation spectrum; we will obtain it using the spin-Hamiltonian with the optimized $SU(2)$ parameters. The $U(1)$ part is optimized by minimizing the total energy; the optimization

is performed under the condition that single-particle wave functions are single-valued; when spin-vortices are present, this condition yields a nontrivial fictitious magnetic field, and SVILCs arise. Further, we also give an explanation for the suppression of superconductivity in the $x = 1/8$ static-stripe-ordered sample by examining its SVILCs. In Sect. 3, the temperature dependence of the Nernst signal is explained [20] by the fictitious electric field produced by the time-dependence of the $U(1)$ phase [7]. It is indicated that superconductivity occurs at temperatures where small polarons become immobile; then the current below T_c is mainly attributed to SVILCs [21]; thus the change of the sign of the Hall coefficient from positive (by the hole-hopping) to negative (by the SVILCs) is explained; it also explains the negative Hall coefficient observed in the magnetic-field-induced “normal state” [20]. In Sect. 4, we examine the ARPES spectrum by assuming that small polarons are not formed in the surface region. We will show that the “Fermi-arc” [19] and the “kink” [22] arise from the interaction between the electronic state in the surface region and that in the bulk. In Sect. 5, we will conclude the present work.

2 Spin-vortices and Spin-vortex-induced Loop Currents

Throughout the present work, we assume that the electronic state for conduction electrons in the CuO_2 plane in the bulk of the cuprate is described as that for a system with strong on-site Coulomb repulsion and strong hole-lattice interaction. In this section, we examine it by taking the CuO_2 plane as a two-dimensional square lattice in the xy plane.

Our starting Hamiltonian for the bulk-layer CuO_2 is given by

$$H_{\text{bulk}} = - \sum_{i,j,\sigma} t_{ij} c_{i\sigma}^\dagger c_{j\sigma} + U \sum_j c_{j\uparrow}^\dagger c_{j\uparrow} c_{j\downarrow}^\dagger c_{j\downarrow} + H_{\text{hole+lattice}}, \quad (3)$$

where the first two terms are those of the Hubbard model; the large on-site Coulomb repulsion, $|t_{ij}| \ll U$, is assumed; the third term describes the interaction between holes and underlying lattice, and also lattice vibrations.

Due to $H_{\text{hole+lattice}}$, holes become small polarons at low temperatures. As a consequence, the hopping probability of holes becomes very small. We consider the case where the hopping probability is so small that we may treat the hole-occupied sites as inaccessible sites for electrons in the zeroth approximation. In this situation, the number of accessible sites and that of electrons are equal; we call this situation, the “effectively half-filled situation (EHFS)”. In the EHFS, H_{bulk} is rewritten as

$$H_{\text{EHFS}} = - \sum_{i,j \in \text{acc. sites}, \sigma} t_{ij} c_{i\sigma}^\dagger c_{j\sigma}$$

$$+ U \sum_{j \in \text{acc. sites}} c_{j\uparrow}^\dagger c_{j\uparrow} c_{j\downarrow}^\dagger c_{j\downarrow}. \quad (4)$$

Local moments appear in the present EHFS due to the strong correlation condition $U \gg |t_{ij}|$. Then the ground state is an antiferromagnetic insulator as in the parent compound of the cuprate; thus, we may also call it the “effectively half-filled Mott insulator (EHFMI)” state [5]. However, the EHFMI state differs from the parent compound of the cuprate by an additional assumption; we allow it to have spin-vortices with holes at their centers.

In the EHFMI, we have

$$\langle c_{i\uparrow}^\dagger c_{i\uparrow} + c_{i\downarrow}^\dagger c_{i\downarrow} \rangle = \begin{cases} 1 & \text{if } i \text{ is not occupied by a hole} \\ 0 & \text{otherwise} \end{cases}, \quad (5)$$

where $\langle \hat{O} \rangle$ means the expectation value of an operator \hat{O} .

The above condition is replaced by a more restrictive condition

$$c_{i\uparrow}^\dagger c_{i\uparrow} + c_{i\downarrow}^\dagger c_{i\downarrow} = \begin{cases} 1 & \text{if } i \text{ is not occupied by a hole} \\ 0 & \text{otherwise} \end{cases} \quad (6)$$

in the derivation of the Heisenberg Hamiltonian from the Hubbard Hamiltonian. Note that the difference of the conditions between (5) and (6) is tremendous; the former allows current flow, but the latter does not.

Let us introduce new particle operators, a_j and b_j , so that we can introduce spin-vortices as a prescribed condition;

$$\begin{pmatrix} a_j \\ b_j \end{pmatrix} = e^{i \frac{x_j}{2}} \begin{pmatrix} e^{i \frac{\xi_j}{2}} \cos \frac{\theta_j}{2} & e^{-i \frac{\xi_j}{2}} \sin \frac{\theta_j}{2} \\ -e^{i \frac{\xi_j}{2}} \sin \frac{\theta_j}{2} & e^{-i \frac{\xi_j}{2}} \cos \frac{\theta_j}{2} \end{pmatrix} \begin{pmatrix} c_{j\uparrow} \\ c_{j\downarrow} \end{pmatrix}. \quad (7)$$

The above basis transformation matrix is composed of a $U(1)$ phase factor $e^{i \frac{x_j}{2}}$ and an $SU(2)$ matrix.

Corresponding to (5), we may choose the new particle operators a_j and b_j for the j th site to satisfy,

$$\langle a_j^\dagger a_j + b_j^\dagger b_j \rangle = \begin{cases} 1; \langle a_j^\dagger a_j \rangle \gg \langle b_j^\dagger b_j \rangle & \text{if } j \text{ is not occupied by a hole} \\ 0 & \text{otherwise} \end{cases}. \quad (8)$$

An important point is that the condition $\langle a_j^\dagger a_j \rangle \gg \langle b_j^\dagger b_j \rangle$ is added.

Due to the additional condition, the zeroth ground state is given by

$$|0\rangle = \prod_{i \in \text{acc. sites}} a_i^\dagger |\text{vac}\rangle. \quad (9)$$

Let us calculate the local moments with $|0\rangle$; we have

$$S_x(j) = \frac{1}{2} \langle 0 | c_{j\uparrow}^\dagger c_{j\downarrow} + c_{j\downarrow}^\dagger c_{j\uparrow} | 0 \rangle = \frac{1}{2} \cos \xi_j \sin \theta_j,$$

$$S_y(j) = \frac{i}{2} \langle 0 | -c_{j\uparrow}^\dagger c_{j\downarrow} + c_{j\downarrow}^\dagger c_{j\uparrow} | 0 \rangle = \frac{1}{2} \sin \xi_j \sin \theta_j, \quad (10)$$

$$S_z(j) = \frac{1}{2} \langle 0 | c_{j\uparrow}^\dagger c_{j\uparrow} - c_{j\downarrow}^\dagger c_{j\downarrow} | 0 \rangle = \frac{1}{2} \cos \theta_j.$$

This indicates that ξ_j and θ_j are identified as the azimuth and polar angles of the local moment at the j th site.

We optimize the $U(2)$ parameters ξ and θ whose values at the j th site are given by $\xi_j = \xi(\mathbf{r}_j)$ and $\theta_j = \theta(\mathbf{r}_j)$, respectively, so that the interaction energy of the local moments is minimized with prescribed winding numbers for spin-vortices, where the winding number around the i th site is defined as

$$w_i[\xi] = \frac{1}{2\pi} \oint_{C_i} \nabla \xi \cdot d\mathbf{r} \quad (11)$$

where C_i is a closed path with its center at the i th site that includes only the vortex at the i th site. Nonzero w_i means that $\xi(\mathbf{r})$ is a multivalued function of the coordinate \mathbf{r} , and a spin-vortex exists with its center at i .

In the cuprate problem, the localized moments are essentially lying in the CuO_2 plane; thus, we just put $\theta_j = \pi/2$ for all sites in this work to make the problem simpler. With this simplification, (7) becomes

$$\begin{pmatrix} a_j \\ b_j \end{pmatrix} = \frac{e^{i\frac{\xi_j}{2}}}{\sqrt{2}} \begin{pmatrix} e^{i\frac{\xi_j}{2}} & e^{-i\frac{\xi_j}{2}} \\ -e^{i\frac{\xi_j}{2}} & e^{-i\frac{\xi_j}{2}} \end{pmatrix} \begin{pmatrix} c_{j\uparrow} \\ c_{j\downarrow} \end{pmatrix}. \quad (12)$$

Using the above new particle operators, the hopping term in H_{EHFS} is written as

$$\begin{aligned} K_{\text{acc}} = & - \sum_{k,j \in \text{acc. sites}} t_{kj} e^{i\frac{1}{2} \int_j^k \nabla \chi \cdot d\mathbf{r}} \\ & \times \left[\cos \frac{\xi_k - \xi_j}{2} (a_k^\dagger a_j + b_k^\dagger b_j) \right. \\ & \left. - i \sin \frac{\xi_k - \xi_j}{2} (a_k^\dagger b_j + b_k^\dagger a_j) \right]. \end{aligned}$$

A remarkable point is that transfer integrals acquire phase factors, $e^{i\frac{1}{2} \int_j^k \nabla \chi \cdot d\mathbf{r}}$, that would be introduced by the Peierls substitution if a magnetic field with the vector potential

$$\mathbf{A}_{\text{fic}} = \frac{\hbar}{2q} \nabla \chi, \quad (13)$$

is applied, where q denotes the charge on the charge carrier. If \mathbf{A}_{fic} is not trivial, it gives rise to a *fictitious magnetic field* [5].

Now, let us construct an optimal Hartree–Fock field for the Hamiltonian for the following EHFMI state:

$$H_{\text{EHFMI}} = K_{\text{acc}} + U \sum_{j \in \text{acc. sites}} a_j^\dagger a_j b_j^\dagger b_j. \quad (14)$$

For the optimization of the parameter ξ , we need to calculate the interaction energy between local moments. For that purpose, we use the spin-Hamiltonian derived by taking the on-site Coulomb interaction term as the zeroth Hamiltonian and K_{acc} as a perturbation; we also employ the approximation in which the condition in (8) is replaced by the following:

$$a_i^\dagger a_i + b_i^\dagger b_i = \begin{cases} 1 & \text{if } i \text{ is not occupied by a hole} \\ 0 & \text{otherwise} \end{cases}. \quad (15)$$

The above condition is actually equivalent to the one in (6).

The resulting spin-Hamiltonian is [12, 23]

$$\begin{aligned} H_{\text{spin}} = & \frac{1}{U} \sum_{k,j \in \text{acc. sites}} t_{jk}^2 \sin^2 \frac{\xi_j - \xi_k}{2} \\ & \times \left(\tilde{S}_k^- \tilde{S}_j^- + \tilde{S}_k^+ \tilde{S}_j^+ - 2\tilde{S}_k^Z \tilde{S}_j^Z - \frac{1}{2} \right) \\ & + \frac{1}{U} \sum_{k,j \in \text{acc. sites}} t_{jk}^2 \cos^2 \frac{\xi_j - \xi_k}{2} \\ & \times \left(\tilde{S}_k^- \tilde{S}_j^+ + \tilde{S}_k^+ \tilde{S}_j^- + 2\tilde{S}_k^Z \tilde{S}_j^Z - \frac{1}{2} \right), \end{aligned} \quad (16)$$

where spin operators, \tilde{S}_j^+ , \tilde{S}_j^- , and \tilde{S}_j^Z are defined as

$$\tilde{S}_j^+ = b_j^\dagger a_j, \quad (17)$$

$$\tilde{S}_j^- = a_j^\dagger b_j, \quad (18)$$

$$\tilde{S}_j^Z = \frac{1}{2} (b_j^\dagger b_j - a_j^\dagger a_j); \quad (19)$$

and the commutation relations for them are

$$[\tilde{S}_j^Z, \tilde{S}_j^\pm] = \pm \tilde{S}_j^\pm, \quad (20)$$

$$[\tilde{S}_j^+, \tilde{S}_j^-] = 2\tilde{S}_j^Z. \quad (21)$$

We optimize ξ through the minimization of

$$\langle 0 | H_{\text{spin}} | 0 \rangle = -\frac{1}{U} \sum_{k,j} t_{jk}^2 \sin^2 \frac{\xi_j - \xi_k}{2}, \quad (22)$$

subject to the prescribed winding numbers for ξ that give rise to spin-vortices.

Spin vortices are introduced as follows: First, we give the initial phase for ξ_j as

$$\xi_j^{\text{init}} = \pi(j_x + j_y) + \sum_M W(j, M) - \sum_A W(j, A), \quad (23)$$

where $j = (j_x, j_y)$ is the two-dimensional coordinate of the j th site. The first term in the r.h.s. describes the antiferromagnetic spin configuration which does not contribute to the

winding number; the second and third terms are those for spin vortices with winding number +1 (called, “meron”), and −1 (called, “antimeron”) [24], respectively, where the function $W(j, M)$ is given by

$$W(j, M) = \tan^{-1} \frac{j_x - M_x}{j_y - M_y}, \quad (24)$$

where $M = (M_x, M_y)$ and $A = (A_x, A_y)$, respectively, indicate two-dimensional coordinates for the center of a meron and the center of an antimeron.

Let us calculate spin-wave excitations. In order to calculate spin-wave excitations, we employ the semiclassical equations of motion method; the linearized equations of motion are obtained as

$$\begin{aligned} -i\dot{\tilde{S}}_k^+ &= [H_{\text{spin}}, \tilde{S}_k^+] \\ &\approx \frac{2}{U} \sum_j t_{kj}^2 \sin^2 \frac{\xi_j - \xi_k}{2} (\tilde{S}_j^- + \tilde{S}_k^+) \\ &\quad - \frac{2}{U} \sum_j t_{kj}^2 \cos^2 \frac{\xi_j - \xi_k}{2} (-\tilde{S}_j^+ + \tilde{S}_k^+), \end{aligned} \quad (25)$$

where the linearization is achieved by the following replacement:

$$\tilde{S}_j^Z \approx -\frac{1}{2}. \quad (26)$$

The spin-wave excited states are expressed as

$$\begin{aligned} |f\rangle &= \frac{1}{\sqrt{2}} \sum_j [(C_j^X(f) - iC_j^Y(f))\tilde{S}_j^+ \\ &\quad + (C_j^X(f) + iC_j^Y(f))\tilde{S}_j^-]|0'\rangle, \end{aligned} \quad (27)$$

where $|0'\rangle$ is the true ground state of the spin Hamiltonian [23].

Then the equation of motion in (25) leads to

$$\begin{aligned} \frac{d}{dt} \langle 0' | -i\tilde{S}_k^+ | f \rangle e^{-i\omega_f t} \\ = \frac{2}{U} \sum_j t_{kj}^2 \langle 0' | \sin^2 \frac{\xi_j - \xi_k}{2} (\tilde{S}_j^- + \tilde{S}_k^+) \\ + \cos^2 \frac{\xi_j - \xi_k}{2} (\tilde{S}_j^+ - \tilde{S}_k^+) | f \rangle e^{-i\omega_f t}. \end{aligned} \quad (28)$$

From the above, two sets of eigenvalue equations for $C_j^X(f)$ and $C_j^Y(f)$ are obtained; if we connect the X component to a nearby Y , and the Y to a nearby X component,

we obtain

$$\text{(Mode I)} \begin{cases} i\omega_f C_k^X(f) = \frac{2}{U} \sum_j t_{kj}^2 \cos(\xi_j - \xi_k) \\ \quad \times (C_j^Y(f) - C_k^Y(f)) \\ i\omega_f C_k^Y(f) = -\frac{2}{U} \sum_j t_{kj}^2 (C_j^X(f) \\ \quad - \cos(\xi_j - \xi_k) C_k^X(f)) \end{cases};$$

if we connect the X component to a nearby X , and the Y to a nearby Y component, we obtain another set,

$$\text{(Mode II)} \begin{cases} \omega_f C_k^X(f) = -\frac{2}{U} \sum_j t_{kj}^2 (C_j^X(f) \\ \quad - \cos(\xi_j - \xi_k) C_k^X(f)) \\ \omega_f C_k^Y(f) = -\frac{2}{U} \sum_j t_{kj}^2 \cos(\xi_j - \xi_k) \\ \quad \times (C_j^Y(f) - C_k^Y(f)) \end{cases}.$$

The magnetic excitation spectra are plotted using the structure factor given by

$$S(\mathbf{k}, \omega) = \sum_f |\tilde{S}_f^+(\mathbf{k})|^2 \delta(\omega - \omega_f), \quad (29)$$

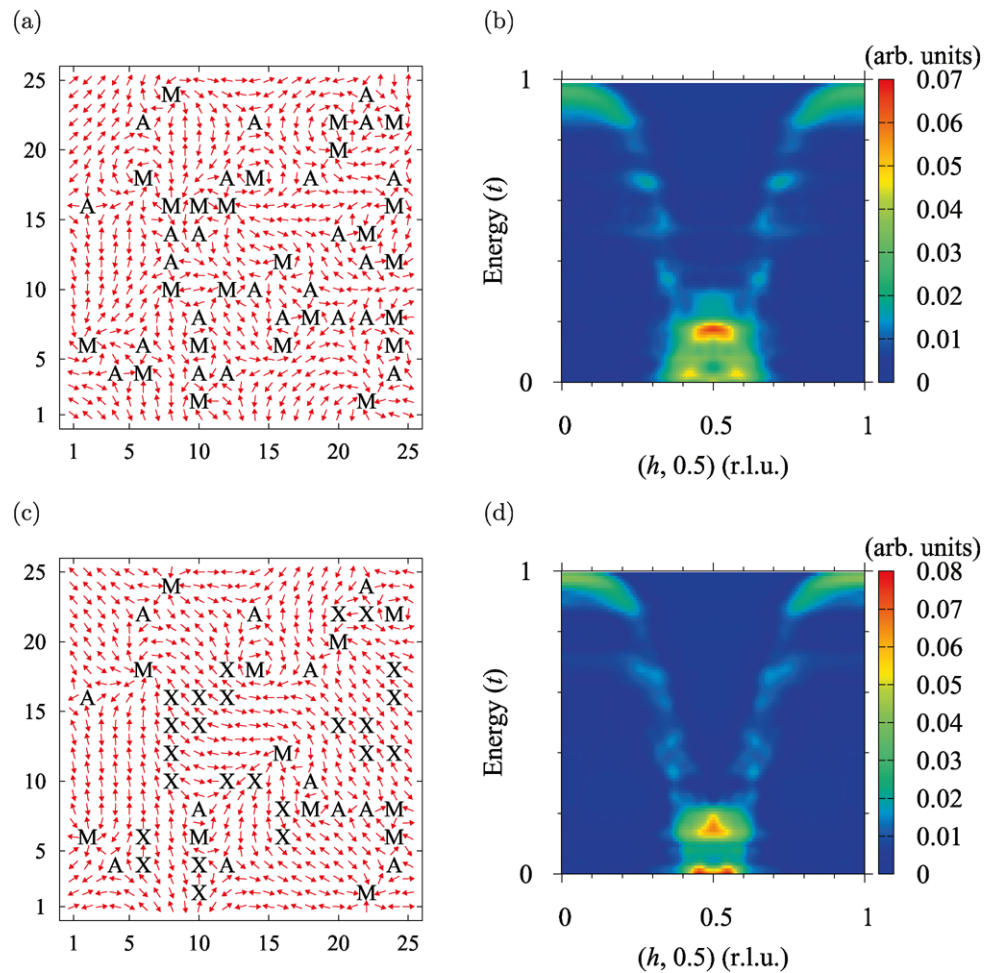
where ω_f is the energy for the spin-wave excited state $|f\rangle$, $\tilde{S}_f^+(\mathbf{k})$ is the Fourier transform of $\langle f | \tilde{S}_j^+ | 0' \rangle$ given by

$$\tilde{S}_f^+(\mathbf{k}) = \frac{1}{\sqrt{N_s}} \sum_j \langle f | \tilde{S}_j^+ | 0' \rangle e^{-\mathbf{k} \cdot \mathbf{r}_j}. \quad (30)$$

In Fig. 1, examples of calculated results are depicted. They contain both contributions from Mode I and Mode II excitations. The nearest-neighbor transfer integral is denoted as t , and take as the unit of energy. The obtained spin-wave excitation structure factor exhibits the hourglass shape with a pronounced resonance peak at $(h, k) = (1/2, 1/2)$. The Mode II excitations account for the dispersion below the resonance peak, and the Mode I excitations do for the rest. In the second row, results for the optimized ξ obtained from ξ^{init} in the first row are depicted. Actually, some of spin-vortices in the initial configuration disappear in the optimized configuration. Due to this reduction of spin-vortices, the splitting of peaks around $(1/2, 1/2)$ at low energies is decreased. The initial spin configurations given by ξ^{init} are usually unstable in the sense that some of the spin-vortices disappear during optimization. We have argued that the hourglass-shaped magnetic excitation spectrum [9–11] is a strong support for the existence of spin-vortices in the previous work [12]. The spin-wave spectrum in Fig. 1 reconfirms that argument.

In Fig. 2, we have depicted cases for spin configurations with a stripe-order and extra holes. A stripe spin configuration is stable in optimization. A square structure of four spin-vortices depicted in spin configurations in the second

Fig. 1 Plots of spin configurations for the spin-vortex model and the spin-wave excitation structure factor $S(\mathbf{k}, \omega)$. Calculations are done in the two-dimensional square lattice with 25×25 sites. 48 holes are randomly distributed; M and A indicates a meron (winding number $+1$ spin-vortex) and an antimeron (winding number -1 spin-vortex), respectively. The result for $S(\mathbf{k}, \omega)$ is symmetrized around $(h, k) = (1/2, 1/2)$ to have the C_4 symmetry, and broadened with Gaussian functions. (a) and (b) results for ξ^{init} ; (c) and (d) results for the optimized ξ from ξ^{init}



and third rows is also stable. Calculated magnetic excitation spectra show a resonance peak and peak-splitting around $(1/2, 1/2)$ at low energies in agreement with experiments [9–11]. The spin configurations that contain a stripe-order reproduce the clear splitting of the $(1/2, 1/2)$ peak at low energies; it suggests that stripe-order exist in the cuprate together with other spin-vortex distributions.

Now we consider the optimization of χ_j in (12). In order to optimize χ , we need to include the itineracy of electrons since its effect appears in the hopping term K_{acc} .

We employ the following mean field Hamiltonian:

$$H_{\text{EHFSS}} = K_{\text{acc}} + U \sum_{j \in \text{acc. sites}} (\langle a_j^\dagger a_j \rangle b_j^\dagger b_j + \langle b_j^\dagger b_j \rangle a_j^\dagger a_j - \langle a_j^\dagger a_j \rangle \langle b_j^\dagger b_j \rangle). \quad (31)$$

The ground state is obtained as a Slater determinant for a filled lower band that is separated from an empty upper band by an energy gap of about U . We call the Slater determinant ground state the “effectively half-filled Slater state (EHFSS).” If the spin configuration is that of the antiferro-

magnet, the Slater determinant state is given by a currentless $|0\rangle$ state.

When spin-vortices exist, the phase χ is a multivalued function; therefore, care must be taken in calculations. We minimize the total energy obtained by the mean field solution under the condition that the transformation matrix in (12) is single-valued with respect to the phase shift $\xi_j \rightarrow \xi_j + 2\pi$ since ξ_j and $\xi_j + 2\pi$ are physically equivalent. This means that the phase χ_j should compensate the sign-change of $e^{\pm \frac{i}{2} \xi_j}$ brought about by the phase shift $\xi_j \rightarrow \xi_j + 2\pi$.

The above single-valuedness condition is satisfied by adopting the following constraint:

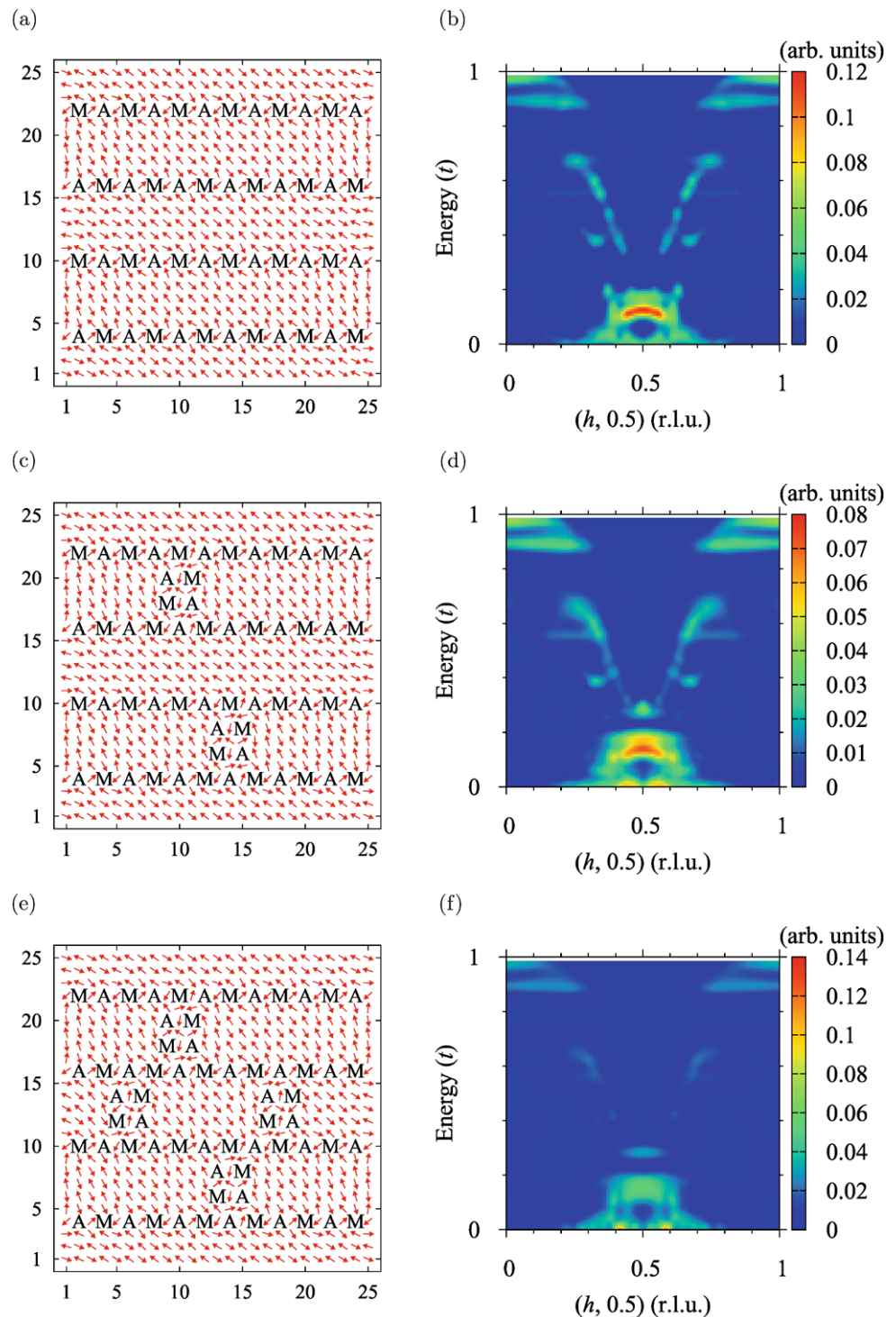
$$w_i[\xi] + w_i[\chi] = \text{even number}, \quad (32)$$

where $w_i[\chi]$ is the winding number for χ defined by

$$w_i[\chi] = \frac{1}{2\pi} \oint_{C_i} \nabla \chi \cdot d\mathbf{r}. \quad (33)$$

This means that, for example, if a spin-vortex with $w_i[\xi] = 1$ exists, $w_i[\chi]$ has to be an odd integer.

Fig. 2 The same as in Fig. 1 but for different spin configurations. *First row*: a stripe configuration for $x = 1/12$. *Second row*: the same stripe order with 8 additional holes. *Third row*: the same stripe order with 12 additional holes



The total energy depends on $\nabla\chi$; the way to optimize it is described in [8]. The nontrivial \mathbf{A}_{fic} generates a current [5–7], which we call the “spin-vortex-induced loop currents (SVILCs).”

In addition to the magnetic excitations that arise from the local moments, excitations associated with the freedom in choosing χ exist. The states with a different set of

$w_i[\chi]$ generate a different collection of loop currents as seen in Fig. 3. Thus, by choosing $w_i[\chi]$ within the restriction in (32), a variety of current patterns can be generated [5–7]. They are intact as long as the spin-vortices induce them are intact. They are close in energy, thus it is expected that the system will show a very sensitive response to an external magnetic field. Since the freedom in choosing χ gives rise

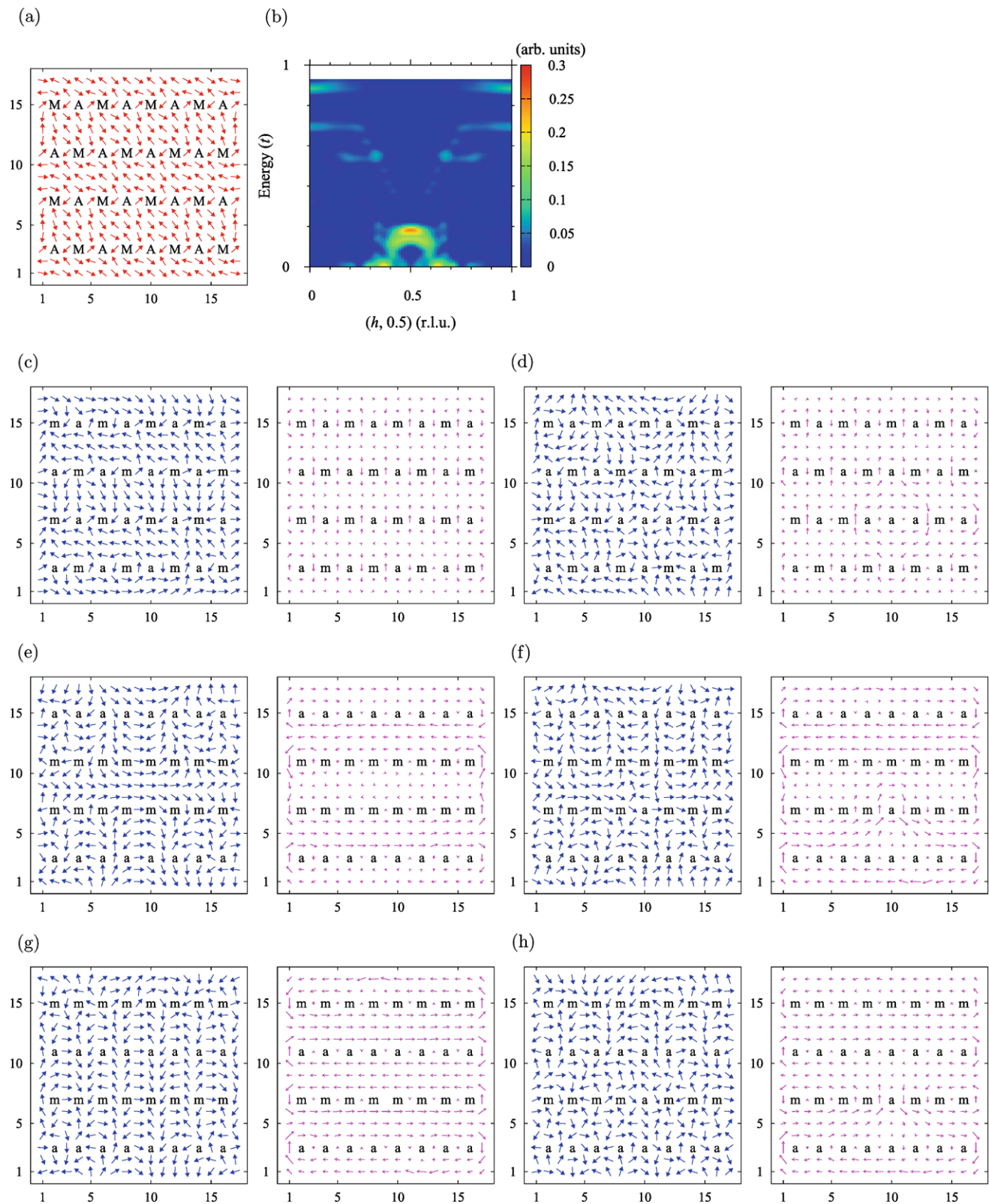


Fig. 3 The static stripe spin configuration for the $x = 1/8$ sample and its current in the spin-vortex model. A 17×17 lattice with the closed boundary condition is employed. **(a)** The spin-configuration. **(b)** The magnetic excitation spectrum for the spin configuration in **(a)**. **(c)–(h)** Results obtained by employing various winding numbers for χ with

the spin configuration in **(a)**; the *left figure* depicts $(\cos \chi, \sin \chi)$ and the *right one* the resulting electric current density (note that $q < 0$). “m” and “a” indicate that the winding numbers $w_i[\chi]$ around them are $w_i = +1$ and $w_i = -1$, respectively

to the freedom in current patterns, we may say that the low energy charge-degree-of-freedom is described by the corrective coordinate χ . This interpretation reminds us of a suggestion that the spin-charge separation is happening in the cuprate [25].

The recent polar Kerr-effect measurement in $\text{YBa}_2\text{Cu}_3\text{O}_{6+x}$ (YBCO) strongly suggests that stable loop currents exist in the pseudogap phase [1, 2]. Actually, there are two kinds of experiments in it. In the first kind, the sample was first cooled to 4.2 K in a +4 T field; then the field was turned off at 4.2 K; and the measurements were done while warming the sample; a finite Kerr signal was observed up to around T^* . This experimental observation can be interpreted that the SVILCs are created at 4.2 K and persist up to the pseudogap temperature T^* . According to the EXAFS experiment [14], the pseudogap temperature is regarded as temperature where small polarons are formed; thus, spin-vortices with small polarons as their cores become stable below this temperature. The fact that the sign of the signal was reversed if the applied field direction is in accordance with the loop current origin of the effect.

In the second kind, the sample was “trained” in a 4 T field at room temperature, first; then the field was turned off, and the sample was cooled in a small field (+60 Oe or –60 Oe) to 4.2 K; lastly, the measurements were done in a zero field warm-up. The results showed that the memory of the trained field at room temperature persists, and the effect of the small field was only limited at temperatures below T_c ; this suggests that even at room temperature, spin-vortices exist although small polarons are not fully-developed. The applied strong magnetic field will create diamagnetic loop currents as eddy currents, then spin-vortices may be created at the same time; these spin-vortex+loop-current complexes will be stable enough to survive to be observed in the later measurement. Below the temperature T_c , the effect of currents created by the ± 60 Oe field was observed; we will come back to this small field effect later.

The static-stripe order is observed in LBCO at $x = 1/8$ [26]; the stability of this configuration probably comes from the structural reason. A remarkable point is that the superconductivity is significantly suppressed in this sample. If the supercurrent arises from SVILCs, ordered-stripe configuration will yield a net zero current since each loop current contributes to an equal amount of current in one and its opposite directions along (not in) the stripe. This situation is depicted in Fig. 3; when only “m”s or “a”s are arranged in each as in Figs. 3(e) and (g), noticeable currents flow occur between the lines. However, current in one direction is canceled by another in the other direction, thus the total current vanishes. When one of the winding number in a line is reversed as see in Figs. 3(d), (f), and (g), a circulating current arises around it; however, it is localized, thus will not contribute to a macroscopic current.

3 Nernst Signal from the Flow of the Loop Currents

In the previous section, we assume that holes are immobile. In this section, we consider the case where holes move slowly by an applied temperature gradient with keeping spin-vortices and loop-currents around them. This slow motion of holes produces a flow of loop currents, and give rise to a time-dependence in \mathbf{A}_{fic} .

The time-dependence of \mathbf{A}_{fic} generates a *fictitious electric field* [6]

$$\mathbf{E}_{\text{fic}} = -\frac{1}{c} \frac{\partial}{\partial t} \mathbf{A}_{\text{fic}} = -\frac{\hbar}{2q} \nabla \dot{\chi} \quad (34)$$

in the same manner as a time-dependence of the real vector potential produces an electric field.

It has been pointed out that this \mathbf{E}_{fic} explains an enhanced Nernst signal e_N observed in the pseudogap phase of the cuprate [6, 27–29], where e_N is defined as

$$e_N = \frac{E_y}{-\partial_x T}. \quad (35)$$

In Fig. 4, the experimental setup is depicted; the magnetic field is applied in the z -direction, the temperature gradient is in the x -direction with $\partial_x T < 0$, and the induced electric field is in the y -direction; E_y , arises as an electric field that compensates the y component of the fictitious electric field \mathbf{E}_{fic} , which is generated by the accumulation of charges on surfaces normal to the y -direction.

The current direction of each loop-current is either paramagnetic or diamagnetic to an applied magnetic field (see Fig. 5). In our previous work, we have considered the case where all loop currents are diamagnetic [6] with winding number +1. In that case, the Nernst signal is obtained as

$$e_N^d = \frac{\hbar v n_d}{-2e \partial_x T}, \quad (36)$$

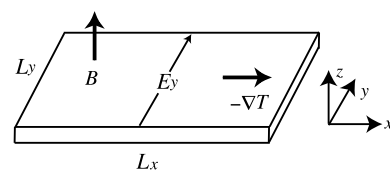


Fig. 4 Experimental set-up for the Nernst effect measurement

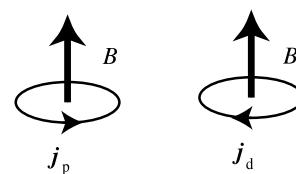


Fig. 5 Paramagnetic-loop-current \mathbf{j}_p and diamagnetic one \mathbf{j}_d . The former is considered as a magnetic moment in the direction of the applied magnetic field, and the latter is that in the opposite direction

where v is the average velocity of spin-vortex flow, h is Planck's constant, and n_d is the surface density of the diamagnetic loop currents.

Since the magnetic field energy of the current density \mathbf{j} in a magnetic field is given by

$$U_m = \frac{1}{2c} \int d^3r \int d^3r' \mathbf{j}(\mathbf{r}') \cdot \mathbf{A}(\mathbf{r}), \quad (37)$$

where \mathbf{A} is the vector potential for the total (external + loop-current-induced) magnetic field, diamagnetic loop currents are energetically favorable; thus, the above treatment is justifiable.

However, when the number density of loop currents is small we need to include the contribution from paramagnetic loop currents (\mathbf{j}_p in Fig. 5) as well; this is because that when the number density of loop currents is small, they are basically isolated magnetic moments produced by \mathbf{A}_{fic} ; in this situation, the energy of magnetic moments in an external magnetic field is given by

$$U_p = - \sum_i \mathbf{m}_i \cdot \mathbf{B}_i \quad (38)$$

where \mathbf{m}_i is the magnetic moment that corresponds to the loop current centered at the i th site. In contrast to U_m , this contribution favors paramagnetic-loop-currents.

If we estimate the paramagnetic-loop-current contribution in a similar manner as for the diamagnetic contribution by assuming their winding numbers are all -1 , it is given by

$$e_N^p = \frac{h v n_p}{2e \partial_x T}, \quad (39)$$

where n_p is the surface density of the paramagnetic loop currents.

Then the Nernst signal is the sum of the two contributions given by

$$e_N = \frac{h v (n_d - n_p)}{2e |\partial_x T|}. \quad (40)$$

The Nernst effect measurements have observed that a negative Nernst signal starts to appear at around T^* ; and the negative signal turns to the positive one as the temperature is decreased [20]. The expression in (40) indicates that this sign change is explained if a crossover from $n_p > n_d$ to $n_p < n_d$ occurs as the temperature is decreased. In the following, we consider this crossover in an ad hoc manner.

For simplicity, we assume that all holes become centers of loop currents; thus, we have

$$n_s = n_p + n_d. \quad (41)$$

A very simplified parameterization for the paramagnetic contribution in (38) may be given by

$$U_p \approx -A_1(n_p - n_d), \quad (42)$$

where A_1 is a positive parameter linearly depends on the applied magnetic field; this term describes an energy gain for paramagnetic-loop-currents and loss for diamagnetic ones.

When the number density of loop currents becomes large, the current density becomes large; then magnetic energy U_m that contains a term of quadratic dependence with respect to the current density becomes dominant. This will mean that when the current density becomes sufficiently large, diamagnetic-loop-currents will be dominant; we include this effect by adding an energy loss term for paramagnetic-loop-currents.

Overall, we come up with the following function for n_p and n_d that are used to describe the above-mentioned crossover; i.e., n_p and n_d are obtained by minimizing,

$$E_m = -A_1(n_p - n_d) + A_2 n_p^2, \quad (43)$$

where the second term with a positive parameter A_2 describes the energy loss for the paramagnetic-loop-current generation.

The minimization condition for E_m with respect to n_d yields

$$n_d = \begin{cases} 0 & \text{if } n_s < A_1/A_2 \\ n_s - A_1/A_2 & \text{if } n_s \geq A_1/A_2 \end{cases}. \quad (44)$$

In our previous work [6], the temperature dependence of the Nernst signal e_N^d is obtained as

$$e_N^d = c_3 T^{-1} e^{-0.5 W_p / k_B T} / (1 + c_2 T e^{-W_p / k_B T}). \quad (45)$$

In order to include n_p contribution, we need to a temperature dependence of n_s ; we express it as

$$n_s = c_4 / (1 + c_2 T e^{-W_p / k_B T}), \quad (46)$$

where c_4 is a fitting parameter. This temperature dependence is obtained by assuming that n_s has the same temperature dependence as the magnetization $-M$ at low temperatures since at low temperature almost all loop currents are expected to be diamagnetic, thus $n_s \approx n_d$ should hold. In our previous work [6], $-M$ is given as

$$-M = c_1 / (1 + c_2 T e^{-W_p / k_B T}); \quad (47)$$

thus, the condition $n_s \approx n_d \propto M$ leads to the n_s given in (46).

The final form of the temperature dependence of the Nernst signal is given by

$$e_N = \begin{cases} -c_3 e^{-0.5 W_p / k_B T} (c_4 T)^{-1} n_s & \text{if } n_s < A_1/A_2 \\ c_3 e^{-0.5 W_p / k_B T} (c_4 T)^{-1} (n_s - \frac{2A_1}{A_2}) & \text{if } n_s \geq A_1/A_2 \end{cases} \quad (48)$$

with n_s given in (46).

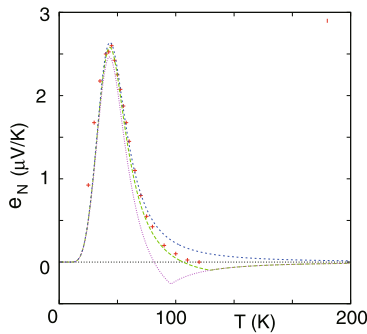


Fig. 6 Temperature dependence of the Nernst signal: Experimental data for $\text{Bi}_2\text{Sr}_2\text{CaCu}_2\text{O}_{8+\delta}$ obtained by Wang et al. [28] are presented by “+.” Parameters $c_2 = 10$ K, $c_3 = 5200$ K, and $W_p/k_B = 300$ K are used for all lines. The fit without including paramagnetic loop currents is given by blue short dashed-line [6]. The fit with including both diamagnetic and paramagnetic loop currents is given by green dashed-line ($c_4 = 0.045$, $A_1/A_2 = 0.0004$); the purple dotted-line is a predicted result if the magnitude of the applied field is tripled ($c_4 = 0.045$, $A_1/A_2 = 0.0012$)

In Fig. 6, the temperature dependence of e_N is depicted. It shows qualitatively similar behaviors as the recent Nernst effect experiment [20]. The zero signal temperature, at which e_N is equal to zero, is shifted to a lower temperature if the magnitude of the applied magnetic field is increased in accordance with the experimental results [20]. Although the argument here is very rough, it qualitatively explain the sign-change of e_N .

4 ARPES Spectrum

The experimental results obtained by ARPES and STS indicate the existence of very mobile holes. These results cannot be explained by the EHFMI state caused by the small polaron formation. Since ARPES and STS results contain a large surface electronic state contribution, the difference of the electronic state in the surface region from that in the bulk may be the reason for this discrepancy; it is plausible that small polarons are not formed in the surface region due to poorer screening of the charge and/or less chemical-bond formation compared to the bulk.

In order to explain the ARPES results in the cuprate, we employ a two-layer model in which the first layer mimics the near surface CuO_2 plane and the second layer that in the bulk. In the surface-layer, the small polaron formation effect is eliminated. We employ a Hubbard model including the first and second nearest neighbor hoppings (the transfer integral for the second and first nearest neighbor hoppings are t'_2 and t'_1 , respectively) with a Coulomb parameter U' .

$$H_{\text{surf}} = - \sum_{i,j,\sigma} t_{ij} c_{i\sigma}^\dagger c_{j\sigma} + U' \sum_j c_{j\uparrow}^\dagger c_{j\uparrow} c_{j\downarrow}^\dagger c_{j\downarrow}. \quad (49)$$

In the bulk-layer, we employ the Hamiltonian H_{EHFSS} in (31) with including the second nearest neighbor hopping (the transfer integral for the second and first nearest neighbor hoppings are t_2 and t_1 , respectively). Those two layers are connected by transfer matrix elements between sites in the first layer to corresponding sites in the second layer (transfer integral is t_3).

$$H_{\text{bulk-surf}} = \sum_{i \in \text{surf}, j \in \text{bulk}, \sigma} t_{ij} (c_{i\sigma}^\dagger c_{j\sigma} + c_{j\sigma}^\dagger c_{i\sigma}). \quad (50)$$

The electronic state in the surface-layer is treated by a mean-field theory [5]. Since the parent compound is a three-dimensional antiferromagnet, it may be reasonable to assume that the antiferromagnetic interaction exists between electrons in the surface and those in the bulk. This interaction is included by choosing the phase ξ_j^{surf} in the surface region so that it transcribes the phase ξ_j^{bulk} in the bulk as

$$\xi_j^{\text{surf}} = \xi_j^{\text{bulk}} + \pi. \quad (51)$$

Now we show that electrons moving in an antiferromagnetic background gives rise to the “Fermi arc” structure. In order to make the discussion clear, we first consider a single-layer, H_{surf} only problem.

We employ a mean field approximation to (49) given by

$$\bar{H}_{\text{surf}} = K_{\text{surf}} + \sum_j (\epsilon_j^a a_j^\dagger a_j + \epsilon_j^b b_j^\dagger b_j) \quad (52)$$

where K_{surf} is the hopping energy term in the surface region; parameters ϵ_j^a and ϵ_j^b are defined as

$$\epsilon_j^a = U' \langle b_j^\dagger b_j \rangle, \quad (53)$$

$$\epsilon_j^b = U' \langle a_j^\dagger a_j \rangle. \quad (54)$$

An analytic solution is obtained for an uniform case where $\langle b_j^\dagger b_j \rangle$ and $\langle a_j^\dagger a_j \rangle$ are constant through the lattice;

$$\epsilon_j^a = \epsilon^a = U' n^b, \quad (55)$$

$$\epsilon_j^b = \epsilon^b = U' n^a. \quad (56)$$

The antiferromagnetic background is taken into account by setting $\xi_j = \pi(j_x + j_y)$. Then the single-particle energies are calculated as

$$\epsilon_{\mathbf{k}}^\pm = 0.5(\epsilon^a + \epsilon^b - 8t'_2 \cos k_x \cos k_y) \pm 0.5\sqrt{(\epsilon^b - \epsilon^a)^2 + 16t_1'^2(\cos k_x + \cos k_y)^2},$$

and the creation operator for the $\epsilon_{\mathbf{k}}^-$ -band is given by

$$d_{\mathbf{k}}^{\dagger} = \frac{-4t_1'(\cos k_x + \cos k_y)a_{\mathbf{k}}^{\dagger} + [\epsilon^b - \epsilon^a - \sqrt{(\epsilon^b - \epsilon^a)^2 + 16t_1'^2(\cos k_x + \cos k_y)^2}]b_{\mathbf{k}}^{\dagger}}{\sqrt{[\epsilon^b - \epsilon^a + \sqrt{(\epsilon^b - \epsilon^a)^2 + 16t_1'^2(\cos k_x + \cos k_y)^2}]^2 + 16t_1'^2(\cos k_x + \cos k_y)^2}},$$

where

$$a_{\mathbf{k}}^{\dagger} = \frac{1}{\sqrt{N_s}} \sum_j a_j^{\dagger} e^{i\mathbf{k} \cdot \mathbf{r}_j}, \quad (57)$$

$$b_{\mathbf{k}}^{\dagger} = \frac{1}{\sqrt{N_s}} \sum_j b_j^{\dagger} e^{i\mathbf{k} \cdot \mathbf{r}_j}, \quad (58)$$

with N_s being the number of sites.

In the mean field solution, the ground state with N electrons and energy E_0^N is given by

$$|\Psi_0^N\rangle = \prod_{\epsilon_{\mathbf{k}}^- \leq 0} d_{\mathbf{k}}^{\dagger} |\text{vac}\rangle, \quad (59)$$

where the origin of the energy is taken at the Fermi level.

Then the occupation number densities n^a and n^b in (55) and (56) are calculated as

$$n^a = \sum_{\epsilon_{\mathbf{k}}^- \leq 0} \frac{1}{N_s} \frac{16t_1'^2(\cos k_x + \cos k_y)}{[\epsilon^b - \epsilon^a - \sqrt{(\epsilon^b - \epsilon^a)^2 + 16t_1'^2(\cos k_x + \cos k_y)^2}]^2 + 16t_1'^2(\cos k_x + \cos k_y)^2},$$

and

$$n^b = \sum_{\epsilon_{\mathbf{k}}^- \leq 0} \frac{1}{N_s} \frac{[\epsilon^b - \epsilon^a - \sqrt{(\epsilon^b - \epsilon^a)^2 + 16t_1'^2(\cos k_x + \cos k_y)^2}]^2}{[\epsilon^b - \epsilon^a - \sqrt{(\epsilon^b - \epsilon^a)^2 + 16t_1'^2(\cos k_x + \cos k_y)^2}]^2 + 16t_1'^2(\cos k_x + \cos k_y)^2},$$

respectively, where $\epsilon^b - \epsilon^a$ has to be determined in a self-consistent manner using the following equation:

$$\epsilon^b - \epsilon^a = \sum_{\epsilon_{\mathbf{k}}^- \leq 0} \frac{U}{N_s} \frac{16t_1'^2(\cos k_x + \cos k_y) - [\epsilon^b - \epsilon^a - \sqrt{(\epsilon^b - \epsilon^a)^2 + 16t_1'^2(\cos k_x + \cos k_y)^2}]^2}{[\epsilon^b - \epsilon^a - \sqrt{(\epsilon^b - \epsilon^a)^2 + 16t_1'^2(\cos k_x + \cos k_y)^2}]^2 + 16t_1'^2(\cos k_x + \cos k_y)^2}.$$

In the sudden approximation with neglecting the matrix element effects, the ARPES intensity is proportional to

$$I(\mathbf{k}, \omega) = \sum_{s, \sigma} |\langle \Psi_s^{N-1} | c_{\mathbf{k}\sigma} | \Psi_0^N \rangle|^2 \times \delta(\hbar\omega - E_s^{N-1} - E_{\text{kin}} + E_0^N), \quad (60)$$

where

$$c_{\mathbf{k}\sigma} = \frac{1}{\sqrt{N_s}} \sum_j c_{j\sigma} e^{-i\mathbf{k} \cdot \mathbf{r}_j}, \quad (61)$$

E_{kin} is a kinetic energy of the emitted electron, and $|\Psi_s^{N-1}\rangle$ is a state with $N - 1$ electrons with energy E_s^{N-1} .

Customarily, the ARPES intensity is compared with the single-particle spectral function

$$A(\mathbf{k}, \omega) = \sum_s |\langle \Psi_s^{N-1} | d_{\mathbf{k}} | \Psi_0^N \rangle|^2 \times \delta(\hbar\omega - E_s^{N-1} + E_0^N), \quad (62)$$

$$= \delta(\hbar\omega - \epsilon_{\mathbf{k}}^-). \quad (63)$$

However, in the present case, the observed intensity is not directly connected to the single-particle spectral function, but with a factor $R_{\mathbf{k}}$;

$$I(\mathbf{k}, \omega) = R_{\mathbf{k}} \delta(\hbar\omega - E_{\text{kin}} - \epsilon_{\mathbf{k}}^-), \quad (64)$$

where $R_{\mathbf{k}}$ is given by

$$R_{\mathbf{k}} = |\langle \text{vac} | c_{\mathbf{k}\uparrow} d_{\mathbf{k}+\mathbf{Q}}^\dagger | \text{vac} \rangle|^2 + |\langle \text{vac} | c_{\mathbf{k}\downarrow} d_{\mathbf{k}}^\dagger | \text{vac} \rangle|^2$$

$$= \frac{[\epsilon^b - \epsilon^a - \sqrt{(\epsilon^b - \epsilon^a)^2 + 16t_1'^2(\cos k_x + \cos k_y)^2} - 4t_1'(\cos k_x + \cos k_y)]^2}{[\epsilon^b - \epsilon^a - \sqrt{(\epsilon^b - \epsilon^a)^2 + 16t_1'^2(\cos k_x + \cos k_y)^2}]^2 + 16t_1'^2(\cos k_x + \cos k_y)^2}.$$

Actually, $R_{\mathbf{k}}$ gives rise to an intensity transfer in the \mathbf{k} -space. In the limit $|\epsilon^a - \epsilon^b| \rightarrow 0$, it is a step function;

$$\lim_{|\epsilon^a - \epsilon^b| \rightarrow 0} R_{\mathbf{k}} = \begin{cases} 0 & \text{for } \cos k_x + \cos k_y < 0 \\ 2 & \text{for } \cos k_x + \cos k_y > 0 \end{cases}. \quad (65)$$

In general, a small $|\epsilon^a - \epsilon^b|$ value (which occurs for small U' value) produces a large intensity transfer.

In Fig. 7, $\epsilon_{\mathbf{k}}^-$ and $R_{\mathbf{k}}$ around the Fermi energy are depicted for $U' = 8t_1'$ and $U' = 4t_1'$ cases. The Fermi surface is a Fermi pocket centered around $(\pi/2, \pi/2)$. $R_{\mathbf{k}}$ causes the intensity transfer from the right of the $(\pi, 0)$ – $(0, \pi)$ line to the left, thus the intensity in the right of $(\pi, 0)$ – $(0, \pi)$ line is reduced. In the $U' = 8t_1'$ case, the intensity transfer is small. When U' is reduced to $4t_1'$, the transferred intensity is increased, and the simulated result shows a “Fermi arc” that resembles the experimental result. We will use this U' in the following calculations.

Let us come back to the two-layer model with the Hamiltonian

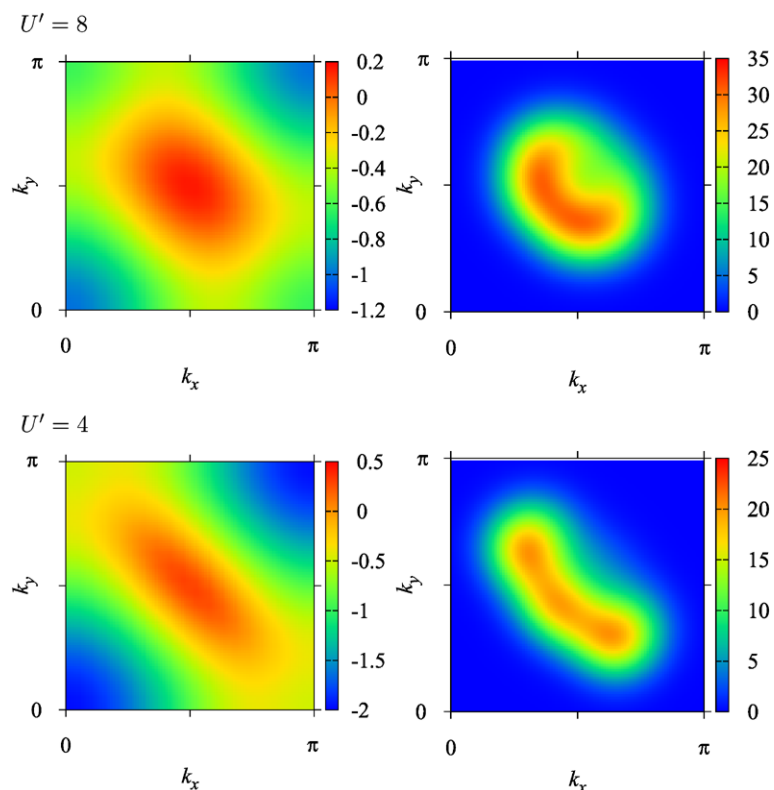
$$H = H_{\text{bulk}} + H_{\text{surf}} + H_{\text{bulk-surf}}. \quad (66)$$

In Fig. 8, the results from the two-layer model are depicted. The Fermi arc is observed from the photoemission intensity from the bulk-layer. The Fermi surface is actually a hole-pocket; however, due to the intensity transfer explained above, the half of the pocket centered around $(\pi/2, \pi/2)$ disappears.

The oscillation of the Hall resistance that indicates an existence of single Fermi pocket of the size that is equal to a combined two Fermi arcs is observed [30]. The subsequent measurement observed that the Hall coefficient is negative [31]. The Fermi pocket around $(\pi/2, \pi/2)$ is hole-like, thus it was concluded the oscillation was due to a different Fermi pocket.

In the present theory, the above experimental results can be interpreted as follows: at temperatures above T_c , both SVILCs in the bulk and mobile holes in the surface region

Fig. 7 Plots for the single-layer model. Contour plots of the single-particle energy $\epsilon_{\mathbf{k}}^-$, and simulated ARPES intensity around the Fermi energy are depicted. *Left:* single-particle energy dispersions; the Fermi energy is taken as the origin ($\epsilon_{\mathbf{k}}^- = 0$). *Right:* Simulated ARPES intensities around the Fermi energy obtained by extracting a region around the Fermi energy from $R_{\mathbf{k}}$ with an energy window $\epsilon_{\mathbf{k}}^- \leq |0.05t_1'|$; contour plot is obtained using 20×20 mesh points. The intensity plots are broadened by Gaussian functions. The unit of energy is t_1' . The parameters are $x = 0.10$, $t_2' = -0.02t_1'$; and $U' = 8t_1'$ for the *first row*, and $U' = 4t_1'$ for the *second row*



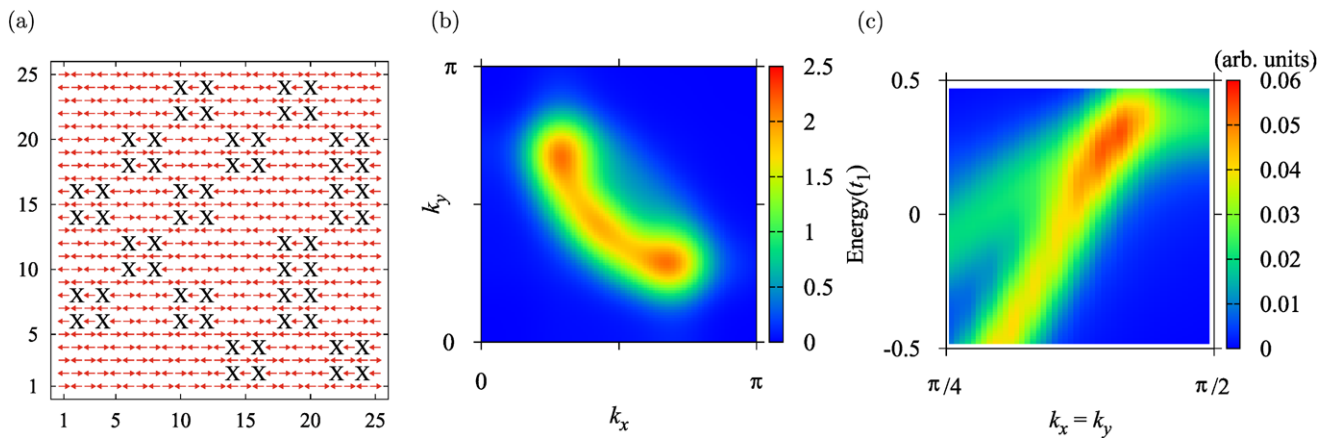


Fig. 8 Plots for the results from the two-layer model. (a) The spin configuration in the bulk layer; 60 holes are in a 25×25 lattice. (b) Fermi surface for the surface-layer; the energy range is from 0.376 to 0.467, where the latter is the Fermi energy. (c) The ARPES spectrum along

$(0, 0) - (\pi/2, \pi/2)$ directions; the intensity of spectrum from the bulk-layer is reduced by half, arbitrarily. The intensity plots are broadened by Gaussian functions. Parameters are $t_1 = t'_1 = 1$, $t_2 = t'_2 = -0.2$, $t_3 = 0.001$, $U = 8$, $U' = 4$

will contribute to electric current. When the temperature is close to T_c , the former dominates; thus, the Hall coefficient is negative. The electrons in the Fermi surface are those in the surface region; they produce a Fermi pocket and explains both the observed Hall resistance oscillation and Fermi-arc structure.

The kink of the dispersion is also noticed in Fig. 8; it arises from the interaction between the electronic state in the surface and that in the bulk. Actually, the kink position corresponds to the crossing energy of the bulk and surface dispersions. It has been observed that isotope effect is negligible for the kink energy. The present interpretation does not require phonons, thus agrees with it [18].

5 Concluding Remarks

In order to explain the anomalous phenomena observed in the pseudogap phase, we have employed a new type of Hartree–Fock fields that is suitable for systems with local moments from itinerant electrons. For the parent compound of the cuprate, it coincides with the band insulator description for the half-filled antiferromagnetic insulator by Slater [15]. It contains three position-dependent parameters to be optimized (ξ , θ , and χ in (7)). The two of them describe the $SU(2)$ part of the basis transformation matrix, and should be optimized by minimizing the interaction energy between local moments.

For the electric current generation, the $U(1)$ phase χ is the most important one. It has to be optimized under the condition given in (32). This dependence of the $U(1)$ phase on the $SU(2)$ part gives rise to an “electromagnetic field” whose vector potential is given in (13).

The appearance of the *fictitious electromagnetic field* is due to the way we solve the problem; namely, we solve it by

constructing a Hartree–Fock field with the collective coordinates θ , ξ , and χ . If we could solve the problem directly without relying on the Hartree–Fock field, the fictitious electromagnetic field would not appear. The situation here is similar to the appearance of a fictitious magnetic field in the dynamical Jahn–Teller problem [32–34]; if we solve the problem by employing the Born–Oppenheimer approximation, we need to include the fictitious magnetic field; however, such a field is not necessary if it is solved directly with including the electron and nuclear degrees of freedom all together.

The merit of introducing the above Hartree–Fock field is obvious; it simplifies to solve the problem and gives a clear physical picture. In the present construction of the Hartree–Fock field, a part of states in highly-degenerate (or nearly-degenerate) states are extracted by specifying winding numbers $w_i[\xi]$ and $w_i[\chi]$; by doing this we can grasp the fact that the existence of spin-vortices leads to the generation of loop currents. Improved solutions will be obtained by using Hartree–Fock solutions as the zeroth approximation and performing configuration-interaction calculations; however, qualitative features of the low energy physics will not be significantly altered.

The ARPES exhibits two gaps in the Fermi surface [35]. The small energy gap is believed to be due to the Cooper-pair condensation. According to the present work, the large energy gap is formed when the “band-holding” occurs in the electronic state in the surface region due to the antiferromagnetic interaction with local moments in the bulk. This “band-holding” is not a true band-holding, but still causes a similar effect. This “band-holding” is also responsible for the appearance of the Fermi arc due to the \mathbf{k} -space intensity transfer.

The existence of the Fermi-arc means the existence of a spin-texture in the surface region that is transcribed from the

bulk. This also means that electrons in the surface region are under the influence of the fictitious magnetic field induced by the transcribed spin-vortices. When the energy gap by the Cooper-pair condensation is established in the surface region, loop currents induced by the transcribed spin-vortices will be stabilized. Then SVILCs appear in the surface region, and they explain the small field effect observed in the second kind Kerr-effect experiment, in which the small field (± 60 Oe field) imposed during cooling gives rise to a contribution at temperatures below T_c in addition to the 4 T field contribution [1, 2].

The magnetic field effects below T_c in the Kerr-effect experiment and the Nernst experiment can be attributed to the Meissner effect of superconducting states; they are explained due to diamagnetic current generated by a collection of SVILCs in the present work. This correspondence leads to an identification that a macroscopic current generated by SVILCs below T_c is actually a supercurrent of superconducting state in accordance with the recently proposed spin-vortex superconductivity theory [8].

Open Access This article is distributed under the terms of the Creative Commons Attribution Noncommercial License which permits any noncommercial use, distribution, and reproduction in any medium, provided the original author(s) and source are credited.

References

- Xia, J., Schemm, E., Deutscher, G., Kivelson, S.A., Bonn, D.A., Hardy, W.H., Liang, R., Siemons, W., Koster, G., Fejer, M.M., et al.: *Phys. Rev. Lett.* **100**, 127002 (2008)
- Kapitulnik, A., Xia, J., Schemm, E., Palevski, A.: *New J. Phys.* **11**, 055060 (2009)
- Li, Y., Balédent, V., Yu, G., Barišć, K., Hradil, R., Mole, A., Sidis, Y., Steffens, P., Zhao, X., Bourges, P., et al.: *Nature* **468**, 283 (2010)
- Varma, C.: *Nature* **468**, 184 (2010)
- Koizumi, H.: *J. Phys. Soc. Jpn.* **77**, 034712 (2008)
- Koizumi, H.: *J. Phys. Chem. A* **113**, 3997 (2009)
- Koizumi, H.: *J. Phys. A, Math. Theor.* **43**, 354009 (2010)
- Koizumi, H.: *J. Supercond. Nov. Magn.* (2011). doi:10.1007/s10948-011-1159-8
- Hayden, S.M., Mook, H.A., Dai, P., Perring, T.G., Doğan, F.: *Nature* **429**, 531 (2004)
- Tranquada, J.M., Woo, H., Perring, T.G., Goka, H., Gu, G.D., Xu, G., Fujita, M., Yamada, K.: *Nature* **429**, 534 (2004)
- Xu, G., Gu, G.D., Hücker, M., Fauqué, B., Perring, T.G., Regnault, L.P., Tranquada, J.M.: *Nat. Phys.* **5**, 642 (2009)
- Koizumi, H.: *J. Phys. Soc. Jpn.* **77**, 104704 (2008)
- Kivelson, S.A., Bindloss, I.P., Fradkin, E., Oganessian, V., Tranquada, J.M., Kapitulnik, A., Howald, C.: *Rev. Mod. Phys.* **75**, 1201 (2003)
- Zhang, C.J., Oyanagi, H.: *Phys. Rev. B* **79**, 064521 (2009)
- Slater, J.C.: *Phys. Rev.* **82**, 538 (1951)
- Pan, S.H., O'Neal, J.P., Badzey, R.L., Chamon, C., Ding, H., Engelbrecht, J.R., Wang, Z., Eisaki, H., Uchida, S., Gupta, A.K., Ng, K.-W., et al.: *Nature* **413**, 282 (2001)
- Gomes, K.K., Pasupathy, A.N., Pushp, A., Ono, S., Ando, Y., Yazudani, A.: *Nature* **447**, 569 (2007)
- Damascelli, A., Hussain, Z., Shen, Z.-X.: *Rev. Mod. Phys.* **75**, 473 (2003)
- Norman, M.R., Ding, H., Randeria, N., Campuzano, J.C., Yokota, T., Takeuchi, T., Takahashi, T., Mochiku, T., Kadowaki, K., Gupta, P., et al.: *Nature* **392**, 157 (1998)
- Daou, R., Chang, J., LeBoeuf, D., Cyr-Choinière, O., Laliberté, F., Doiron-Leyraud, N., Ramshaw, B.J., Liang, R., Bonn, D.A., Hardy, W.N., et al.: *Nature* **463**, 519 (2010)
- LeBoeuf, D., Doiron-Leyraud, N., Levallois, J., Daou, R., Bonnemaison, J.-B., Hussey, N.E., Balicas, L., Ramshaw, B.J., Lia, R., Bonn, D.A., et al.: *Nature* **450**, 533 (2007)
- Lanzara, A., Bogdanov, P.V., Zhou, X.J., Keller, S.A., Feng, D.L., Lu, E.D., Yoshida, T., Eisaki, H., Fujimori, A., Kishio, K., et al.: *Nature* **412**, 510 (2001)
- Koizumi, H.: *J. Phys. Soc. Jpn.* **77**, 123708 (2008)
- Berciu, M., John, S.: *Phys. Rev. B* **69**, 224515 (2004)
- Anderson, P.W.: *Science* **288**, 480 (2000)
- Fujita, M., Goka, H., Yamada, K., Tranquada, J.M., Regnault, L.P.: *Phys. Rev. B* **70**, 104517 (2004)
- Wang, Y., Xu, Z.A., Kakeshita, T., Uchida, S., Ono, S., Ando, Y., Ong, N.P.: *Phys. Rev. B* **64**, 224519 (2001)
- Wang, Y., Li, L., Naughton, M.J., Gu, G.D., Uchida, S., Ong, N.P.: *Phys. Rev. Lett.* **95**, 247002 (2005)
- Wang, Y., Li, L., Ong, N.P.: *Phys. Rev. B* **73**, 024510 (2006)
- Doiron-Leyraud, N., Proust, C., LeBoeuf, D., Levallois, J., Bonnemaison, J.-B., Liang, R., Bonn, D.A., Hardy, W.N., Taillefer, L.: *Nature* **447**, 565 (2007)
- LeBoeuf, D., Doiron-Leyraud, N., Levallois, J., Daou, R., Bonnemaison, J.-B., Hussey, N.E., Balicas, L., Ramshaw, B.J., Liang, R., Bonn, D.A., et al.: *Nature* **450**, 533 (2007)
- Longuet-Higgins, H.C., Öpik, U., Pryce, M.H.L., Sack, R.A.: *Proc. R. Soc. A* **244**, 1 (1958)
- Herzberg, G., Longuet-Higgins, H.C.: *Discuss. Faraday Soc.* **35**, 77 (1963)
- Mead, C.A., Truhlar, D.G.: *J. Chem. Phys.* **70**, 2284 (1979)
- Yoshida, T., Hashimoto, M., Ideta, S., Fujimori, A., Tanaka, K., Mannella, N., Hussain, Z., Shen, Z.-X., Kubota, M., Ono, K., et al.: *Phys. Rev. Lett.* **103**, 037004 (2009)